表 1　骨粗鬆症治療薬の選択例

対象	薬剤選択例
骨折の既往を有する骨折リスクの高い例	アレンドロネート，リセドロネート，ミノドロネート，塩酸ラロキシフェン，バゼドキシフェン酢酸塩，テリパラチド
鎮痛作用を期待する例	カルシトニン製剤
更年期障害を有する例	女性ホルモン
カルシウム不足例	乳酸カルシウム，活性型ビタミン D_3
閉経前症例	活性型ビタミン D_3製剤，ビタミン K_2製剤

ゲン受容体モジュレーター(selective estrogen receptor modulator：SERM，塩酸ラロキシフェン，バゼドキシフェン酢酸塩)，エストロゲンが，骨形成促進薬には副甲状腺ホルモン(テリパラチド)が分類される．活性型ビタミン D_3およびビタミン K_2は骨吸収抑制薬，骨形成促進薬のいずれにも分類されない薬剤である．近年ではその基礎的・臨床的知見から活性型ビタミン D_3は骨吸収抑制薬に，ビタミン K_2は骨形成促進薬に分類される傾向にある．現時点ではわが国の骨粗鬆症治療薬は骨吸収抑制薬が中心である．

ほとんどの骨粗鬆症治療薬は経口薬であり，カルシトニン製剤とテリパラチドが注射製剤である．

ビスホスフォネート薬は消化管から吸収されると速やかに骨に沈着し，一度吸収されたビスホスフォネートは服薬が一定期間行われないで血中濃度が低下しても，骨中に沈着してその有効性を発揮する．そこで服薬間隔を延長することが可能なことから，週1回製剤が開発されている．また，ダイドロネルは2週間服薬，10～12週間休薬を1クールとした周期的間欠投与が行われる．カルシトニン注射製剤は週1回または週2回投与である．

『骨粗鬆症の予防と治療ガイドライン(2006年版)』[4]では掲載，治療効果に従って各骨粗鬆症治療薬の推奨グレードが示された．この推奨グレードに従った実際の薬剤選択では，骨折の既往を有する骨折リスクの高い例では，窒素含有ビスホスフォネート(アレンドロネート，リセドロネート，ミノドロネート)，SERM(塩酸ラロキシフェン，バゼドキシフェン酢酸塩)が第一選択となる(表1)．抗テリパラチドも骨折リスクの高い例が治療対象となる．

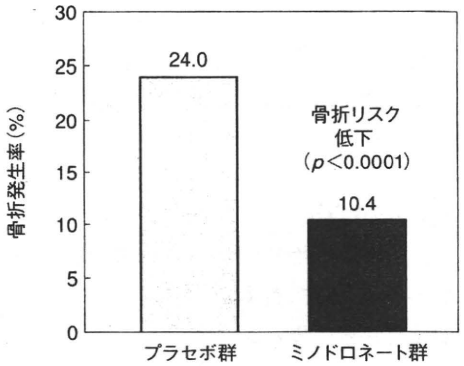

図 2　ミノドロネートの椎体骨折抑制効果[10]
椎体骨折発生率がプラセボ群で24.0%であったのに対し，ミノドロネート群では10.4%で，相対危険度は0.411(95%信頼区間：0.267-0.634)と，59%のリスク低下が示された．

窒素含有ビスホスフォネートのうち，ミノドロネートはわが国で開発され，骨粗鬆症治療薬として認可されたはじめての国産のビスホスフォネートである．2009年，本剤の投与による骨量増加がアレンドロネートと同程度であり，骨吸収マーカーの推移をアレンドロネート群と比較すると，有意にその改善効果が大きく，治療開始後4週で40%以上の低下が報告された[9]．また，骨折予防効果に関して674例の原発性骨粗鬆症患者(平均71歳)を対象に，ミノドロネートとプラセボを比較した2年間にわたる二重盲検比較試験の結果が示され[10]，椎体骨折発生率がプラセボ群で24.0%であったのに対し，ミノドロネート群では10.4%，相対危険度は0.411(95%信頼区間：0.267-0.634)と，59%のリスク低下が示された(図2)．さらに，この骨折リスクの低減は75歳未満の前期高齢者と75歳以上の後期高齢者とで同様であることも最近，報告された．

さらにあらたな骨吸収抑制薬として，抗ランク

ル抗体(デノスマブ)が開発され，2009年，その臨床成績が明らかとなった[11]．半年に一度の60 mgの皮下注射によって，椎体骨折のリスクを68%，大腿骨近位部骨折のリスクを40%，いずれも有意に低下した．

転倒予防とヒッププロテクター

骨粗鬆症治療の目的は“骨折の予防”である．骨折予防には骨粗鬆症の治療，すなわち骨脆弱性の改善のみではなく，転倒防止があげられる．転倒防止のためには，まず転倒リスクと危険因子の評価を行った後，可能な危険因子の改善に取り組む必要がある．これまでの介入研究から，個別の評価と包括的な介入が転倒率を低下させることが明らかになっている[12]．転倒防止のための運動療法では，筋力増強運動とともにバランス訓練が重要である．また，施設入所例でも個別のリスクアセスメント，ケアプラン作成と同時に，多職種連携，薬剤調整，栄養改善，環境調整，職員教育などの包括的介入によって転倒発生率が低減する[13]．

ヒッププロテクターは転倒時に生じる大腿骨近位部への衝撃を和らげるために，衝撃緩衝材が下着に装着されているものである．1993年にその有意な骨折予防効果が報告されて以来，注目されるに至った．しかし，左右片側に装着した臨床試験結果では，装着側のほうが逆に骨折発生率が高く[14]，その骨折予防効果についてはかならずしも一定の結果が得られていない．これは，調査にあたって在宅の高齢者を対象としたか施設入所者を対象としたか，どの程度リスクの高い高齢者を対象としたかで結果が異なるためである．在宅高齢者では継続率が低く効果を得にくいため，施設入所者でスタッフが十分に有用性を理解して装着継続率を高めると，その骨折予防効果が得られる．施設入所者のなかでも骨折リスクの高い例（高頻度転倒例，やせた症例）を対象にした場合には有効である[15]．

おわりに

ロコモティブシンドロームは運動器疾患が原因で介護に至るリスクの高い症候群であり，疾患の重複はさらにリスクを高める．骨粗鬆症は骨折を生じていなければ臨床症状に乏しいが，ひとたび骨折が起こると，さらに骨折リスクが上昇し，骨折が骨折を招来する“負の連鎖”に陥ることとなる．この連鎖を断ち切るために，ロコモティブシンドロームの予防，早期発見・改善が大切である．

文献

1) Dempster, D. W.：Bone remodeling. *In*：Osteoporosis(ed. by Riggs, B. L.). Lippincott-Ravan, Philadelphia, 1995, p.67-91.
2) Fleish, H.(森井浩世監訳)：ビスホスホネートと骨疾患．医薬ジャーナル社，2000.
3) Riggs, B. L. et al.：Clinical trial of fluoride therapy in postmenopausal osteoporotic women：Extended observations and additional analysis. *J. Bone Miner. Res.*, **9**：265-275, 1994.
4) 折茂　肇：骨粗鬆症の予防と治療ガイドライン2006年版．ライフサイエンス出版，2007.
5) 広田孝子：骨粗鬆症患者のカルシウムとビタミンDの栄養状態と骨代謝．*Osteoporos. Jpn.*, **16**：165-169, 2008.
6) Bonaiuti, D. et al.：Exercise for preventing and treating osteoporosis in postmenopausal women. *Cochrane Database Syst. Rev.*, CD000333, 2002.
7) Martyn-St, J. M. et al.：High-intensity resistance training and postmenopausal bone loss：a meta-analysis. *Osteoporos. Int.*, **17**：1225-1240, 2006.
8) Sinaki, M. et al.：Stronger back muscles reduce the incidence of vertebral fractures：a prospective 10 year follow-up of postmenopausal women. *Bone*, **30**：836-841, 2002.
9) Hagino, H. et al.：A double-blinded head-to-head trial of minodronate and alendronate in women with postmenopausal osteoporosis. *Bone*, **44**：1078-1084, 2009.
10) Matsumoto, T. et al.：Effect of daily oral minodronate on vertebral fractures in Japanese postmenopausal women with established osteoporosis：a randomized placebo-controlled double-blind study. *Osteoporos. Int.*, **20**：1429-1437, 2009.
11) Cummings, S. R. et al.：Denosumab for prevention of fractures in postmenopausal women with osteoporosis. *N. Engl. J. Med.*, **361**：756-765, 2009.
12) Gillespie, L. D. et al.：Interventions for preventing falls in older people living in the community. *Cochrane Database Syst. Rev.*, CD007146, 2009.
13) Cameron, I. D. et al.：Interventions for preventing falls in older people in nursing care facilities and hospitals. *Cochrane Database Syst. Rev.*, CD005465, 2010.
14) Kiel, D. P. et al.：Efficacy of a hip protector to prevent hip fracture in nursing home residents：the HIP PRO randomized controlled trial. *JAMA*, **298**：413-422, 2007.
15) Koike, T. et al.：External hip protectors are effective for the elderly with higher-than-average risk factors for hip fractures. *Osteoporos. Int.*, **20**：1613-1620, 2009.

Automated Segmentation Method for Spinal Column Based on a Dual Elliptic Column Model and Its Application for Virtual Spinal Straightening

Shouhei Hanaoka, MD, Yukihiro Nomura, PhD,† Mitsutaka Nemoto, PhD,† Yoshitaka Masutani, PhD,*† Eriko Maeda, MD,‡ Takeharu Yoshikawa, MD, PhD,‡ Naoto Hayashi, MD, PhD,‡ Naoki Yoshioka, MD, PhD,§ and Kuni Ohtomo, MD, PhD*†*

Abstract: Segmentation of vertebral bones in computed tomographic data is important as a first stage of image-based radiological tasks. However, it is a challenging problem to segment an affected spine correctly. In this study, we propose a new method of segmentation of thoracic and lumbar vertebral bodies from thin-slice computed tomographic images. Especially, we focus on a deformable model-based segmentation scheme to confirm the feasibility in clinical data sets with various bone diseases, such as bone metastases and scoliosis. As an application of this algorithm, virtual straightening of the thoracolumbar spine is also performed. Results on a database of 16 patients indicate the applicability of our method to spines affected by scoliosis and multiple bone metastases.

Key Words: segmentation, spine, computed tomography, deformable model, normalization

(*J Comput Assist Tomogr* 2010;34: 156–162)

Segmentation of vertebral bones in computed tomographic (CT) data is important as a first stage of image-based radiological tasks such as radiotherapy planning,[1] evaluation of bone mineral density,[2] or computer-assisted detection (CAD) of bone diseases.[3] So far, several segmentation methods for the spinal column have been reported, including an automated method for all thoracic and lumbar spines.[4] However, segmentation of the spinal column may face difficulties in cases of various diseases such as neoplasm,[5] congenital deformation,[6] or age-related disorders,[7] in which vertebral bones are often destructed, deformed, and/or changed in a signal level. In such cases, segmentation results with errors may have a critical influence on the subsequent processes.

In the segmentation of a diseased spine, we cannot expect the contour of bones to be clear and continuous in any location. It may be torn, ambiguous, or indefinable at all. In such situations, ordinary data-driven methods such as thresholding or region growing often fail. Instead, reliable segmentation algorithms are often constructed based on deformable models such as snakes[8] by assuming a typical or an average structure of the target organ as a model and deforming it.[9] Model-based schemes can use previous anatomical knowledge and complement insufficient contours by the model itself. Hence, it also works for torn or ambiguous bone contours.

However, it is not simple to design a model with enough flexibility for various clinical data sets. In a model-based approach, the model must have enough amount of freedom to describe altered relative positions of vertebrae due to systemic diseases (eg, scoliosis) and local vertebral deformation (eg, compression fracture). However, excessive freedom may increase the model's instability and possibility to sink into local minima. It is always a trade-off between reliability in normal structure extraction and feasibility for abnormal structures.

In this paper, we describe a new method for segmentation of thoracic and lumbar vertebral bodies from thin-slice CT images. Especially, we focus on a deformable model-based segmentation scheme with feasibility in clinical data sets. As an application of the algorithm, virtual straightening of the thoracolumbar spine was performed. These algorithms were evaluated with clinical CT images of cases with bone metastases, scoliosis, and without bone diseases.

MATERIALS AND METHODS

Segmentation Overview

Our segmentation method has 4 steps (Fig. 1). The first step is a preprocessing to determine the initial condition of the model. Then, the model fitting is performed, and all vertebral bodies are segmented as an elliptic cylinder. In the last step, the cylinder is partitioned into individual vertebral bodies.

Design of the Model

The model consists of 2 elliptic columns (Fig. 2A). The first column, B, approximates the vertebral bodies and intervertebral disks, whereas the second column, C, represents the spinal canal. They can be deformed by changing parameters so that they can fit to the given CT images. In segmentation of vertebral bodies, modeling of the canal column C is not essential. However, it makes the model more stable and tolerant of pathologic bone changes, especially for axial rotational transformation of the vertebrae.

An axial cross section of the model is illustrated in Figure 2B. It is composed of 2 circumscribing ellipses sharing their minor axes. The shapes and positions of these ellipses are determined by 7 parameters as follows: transverse and longitudinal diameters of the vertebral column ellipse ($T_B[z]$, $L_B[z]$), those of the spinal canal ellipse ($T_C[z]$, $L_C[z]$), x and y coordinates of the point on which the 2 ellipses circumscribe on the shared minor

From the *Division of Radiology and Biomedical Engineering, Graduate School of Medicine, University of Tokyo; and Departments of †Radiology, ‡Computational Diagnostic Radiology and Preventive Medicine, and §Integrated Imaging Informatics, The University of Tokyo Hospital, Tokyo, Japan.

Received for publication January 29, 2009; accepted May 29, 2009.

Reprints: Shouhei Hanaoka, MD, Department of Radiology, The University of Tokyo Hospital, 7-3-1, Hongo, Bunkyo-ku, Tokyo, Japan 113-8655 (e-mail: hanaoka-tky@umin.ac.jp).

Sources of support: None.

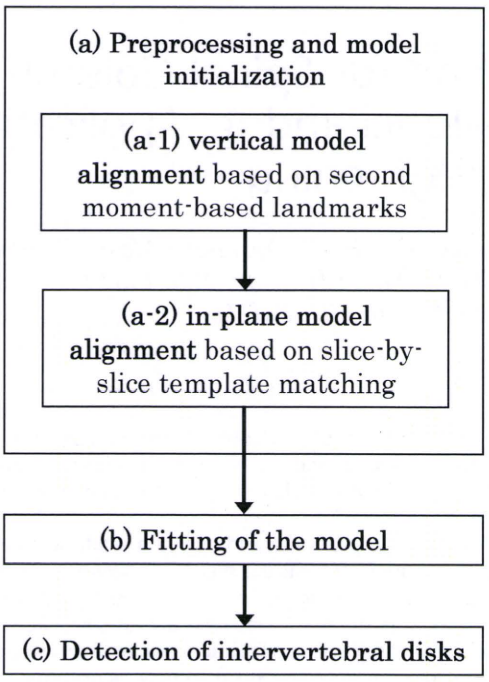

FIGURE 1. Flow chart of segmentation algorithm.

axis ($P_x[z]$, $P_y[z]$), and the orientation angle of the minor axis around the z-axis (z).

We define these parameters discretely on several slices at $z = z_1, z_2, \ldots, z_n$ called *control slices*. z_1 represents the level of the upper border of the model, z_n represents the level of the lower border, and others are placed at a regular interval initially. We used 8 control slices (n = 8) for this study. The parameters of all other slices are determined by cubic spline interpolation.

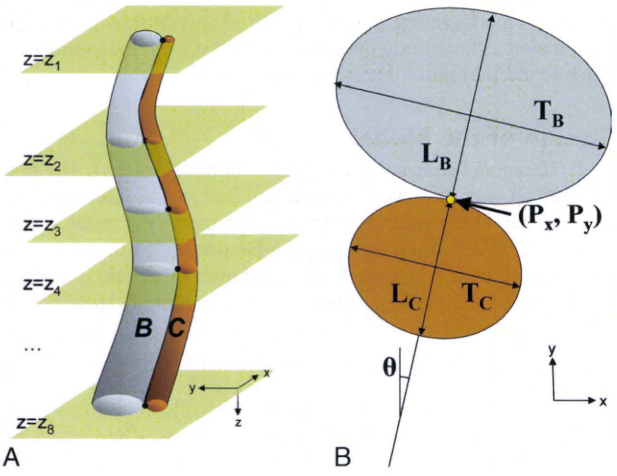

FIGURE 2. Elliptic column model consisting of the vertebral bodies, the intervertebral disks, and the spinal canal. Elliptic column model controlled in 8 control slices (A) from a left lateral view (B). Horizontal cross section of the model.

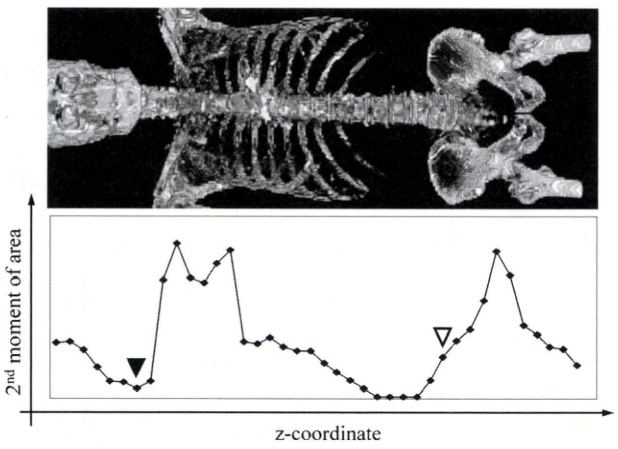

FIGURE 3. Segmented bone structure and second moment of the segmented area.

Detail of the Algorithm

Preprocessing and Model Initialization

Vertical Model Alignment Based on Second Moment–Based Landmarks

First of all, the body trunk region is extracted by means of thresholding with −500 Hounsfield units, 2-dimensional (2D) labeling, and the largest connected component extraction in each slice.

Then, z coordinates of 2 anatomical landmarks, the upper border of the iliac crest and the middle neck, are estimated. The estimation criteria are based on the second moments of area of the bone structure (Fig. 3). After rough extraction of the bone structure with a threshold of 300 Hounsfield units, the second

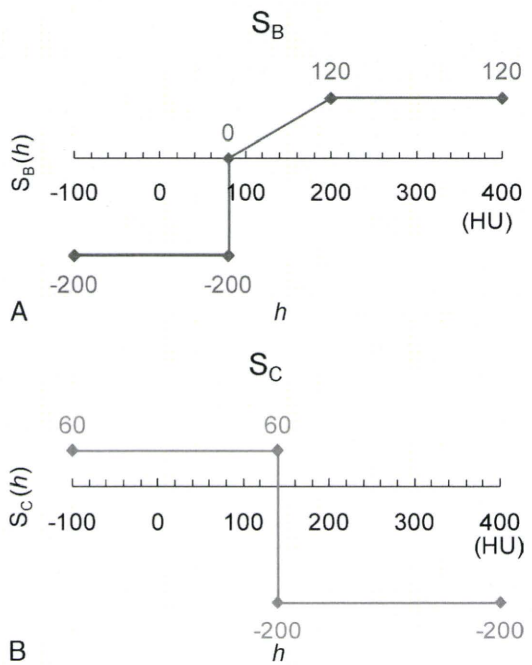

FIGURE 4. Evaluation functions for model fitting. A, S_B for column B. B, S_C for the spinal canal C. The variable h is the CT value of the given voxel.

moment of area around the z-axis is calculated on discrete axial slices. Based on these values, $M(z)$, the level of the upper border of the iliac crest z_{IC} and the middle neck level z_{neck} are estimated as follows:

$$Z_{IC} = sup\left\{z|M(z) < \frac{1}{3}\max_{z<z'} M\left(z'\right)\right\} \quad (1)$$

$$Z_{neck} = \arg\min_{z} M(z). \quad (2)$$

The level z_{IC} is the lowest level that has a smaller moment than one third of the maximal moment of the pelvic bone (ie, bone structure no upper than z_{IC}) used to detect the upper border of the pelvic bone. On the other hand, level z_{neck} is designed to detect the middle neck, which is expected to have the lowest moment in the body.

Finally, the initial values of z_1 and z_n are determined based on the values of Z_{IC} and Z_{neck}.

In-Plane Model Alignment Based on Slice-by-Slice Template Matching

In-plane coordinates of $P_x(z_i)$ and $P_y(z_i)$ are estimated based on 2D template matching. This template has a large size (41 × 31 pixels), an elliptic shape, and a higher value around the center, so as to fit to various sizes of the vertebrae. The other parameters are initialized by empirically determined standard values: $T_B = 105$, $L_B = 70$, $T_C = 28$, $L_C = 21$, and $\Theta = 0$.

Fitting of the Model

In preparation for fitting of the model, a median filter is applied to the volume data for noise reduction. The filter kernel is a sphere with a radius of 1.5 voxels. In the model fitting, 8 parameters on 8 control slices are adjusted, which are z_i, $T_B(z_i)$, $L_B(z_i)$, $T_C(z_i)$, $L_C(z_i)$, $P_x(z_i)$, $P_y(Z_i)$, and $\Theta(z_i)$ $(1 \le i \le 8)$. The model fitness for the CT images is determined by an evaluation function, $E_{fitness}$, which is a sum of 2 functions, E_B and E_C. E_B and E_C evaluate the fitness of the 2 elliptic columns, B and C, respectively. That is,

$$E_{fitness} = E_B + E_C = \sum_{x \in B} S_B(f_M(x)) + \sum_{x \in C} S_C(f_M(x)) \quad (3)$$

Here, both terms E_B and E_C are calculated based on CT values of all voxels included in the corresponding elliptic column. $f_M(\mathbf{x})$ is the image function after medial filtering. Functions S_B and S_C (Figs. 4A and B, respectively) evaluate the CT values of each voxel. The function S_B (which evaluates the CT value suitability for vertebral bodies) is designed for the model to fit to the vertebral body as far as possible. S_B is also designed to have an upper limit to avoid adverse effects due to extremely high CT values in the cortical bones. The function S_C (which evaluates the CT value suitability for the spinal canal) is designed as just a binary function so that the model fits to the canal and the surrounding cortical bones. Parameters in these functions are adjusted empirically, considering balance between E_B and E_C.

The fitting of the model is performed as maximization of the evaluation function $E_{fitness}$ by the modified Powell optimization procedure.[10]

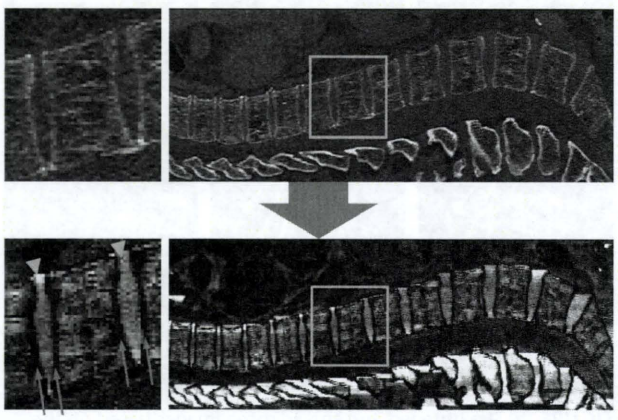

FIGURE 5. Enhancement of the intervertebral disk based on the bottom-hat filter (above). A sagittal image of the original CT data (case 1; under). The filtered result.

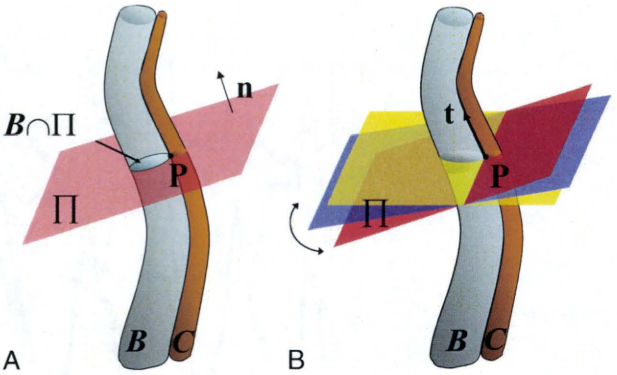

FIGURE 6. Intersection of the column models and search plane.

Detection of Intervertebral Disks

In this phase, intervertebral disks are detected in presegmented spine volume (column B). The tilt angle of each disk is also determined. For this purpose, a disk evaluation function is designed to have 3 variables: 1 is the z coordinate of the disk, and the other 2 represent the tilt angles of the disk plane along the x and y directions.

At first, the disk region is enhanced with a bottom-hat filter, which enhances thin structures with low signals[11] such as intervertebral disks (Fig. 5). The kernel shape is a rectangular parallelepiped, and its size $L_x \times L_y \times L_z$ is as follows: L_x and L_y are 3 voxels, and L_z is determined to be approximately 7.5 mm. The latter is determined based on typical lumbar disk thickness.

Then, the disk evaluation function $D(P_z, n_x, n_y)$ is calculated. The function represents the likelihood of intervertebral disk existence for a given z location and disk orientation.

The function value is calculated at the contact point of 2 elliptic columns on each plane. Let this point be $\mathbf{P}(P_x, P_y, P_z)$. For each point $\mathbf{P}$, plane Π is defined as follows:

$$\Pi : n_x \cdot (x - P_x) + n_y \cdot (y - P_y) + (z - P_z) = 0 \quad (4)$$

Π is a plane passing through $\mathbf{P}$, and its normal vector is $\mathbf{n} = (n_x, n_y, 1)$. The cut plane of $\boldsymbol{B}$ sectioned by Π is approximately an ellipse. Then, a disk-evaluating function D is calculated as a sum of voxel values included in this intersectional ellipse $\boldsymbol{B} \cap \Pi$ (Fig. 6A). That is, letting $f_{BH}(\mathbf{x})$ be the image function after bottom-hat filter,

$$D(P_z, n_x, n_y) = \sum_{x \in B \cap \Pi} f_{BH}(x) \quad (5)$$

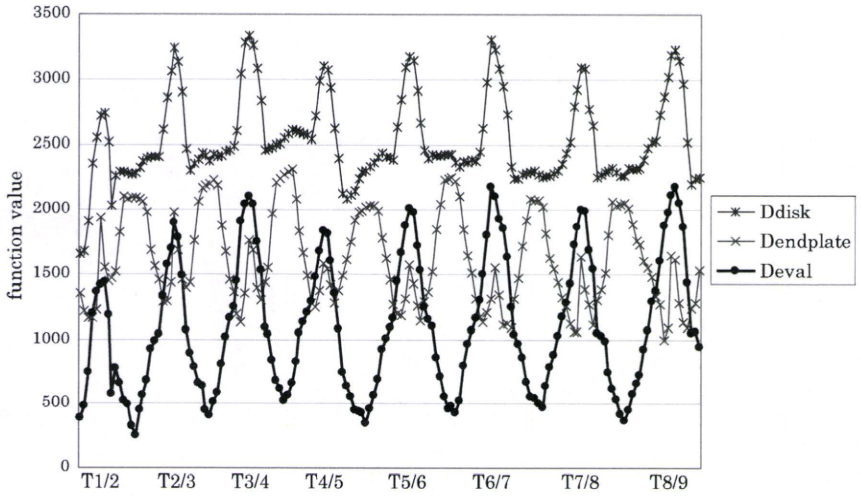

FIGURE 7. Example of D_{disk}, $D_{endplate}$, and D_{eval} (case 5).

D becomes larger if the ellipse $\boldsymbol{B} \cap \Pi$ corresponds to an intervertebral disk.

For stable disk detection, in addition, our algorithm uses information about endplates. An endplate is a thin structure with very low value in $f_{BH}(\mathbf{x})$. An intervertebral disk is sandwiched by 2 endplates (Fig. 5). For every z coordinate, likelihood of both the intervertebral disk and the endplate are evaluated by 2 functions, D_{disk} and $D_{endplate}$, respectively. They are calculated as follows:

$$D_{\text{disk}}(P_z) = \max_{n_x} \max_{n_y} D(P_z, n_x, n_y) \tag{6}$$

$$D_{\text{endplate}}(P_z) = \min_{n_x} \min_{n_y} D(P_z, n_x, n_y) \tag{7}$$

For every point **P**, D is evaluated within the sufficient range of **n** to find the maximum (ie, D_{disk}) and the minimum ($D_{endplate}$) of D (Fig. 6B).

$D_{disk}(P_z)$ is a function that evaluates likelihood of existence of an intervertebral disk around the level $z = P_z$. Therefore, $D_{disk}(P_z)$ is expected to have a local maximum at the z coordinates of each intervertebral disk. On the other hand, the $D_{endplate}$ is expected to have a local minimum at the z coordinate of each endplate.

Supposing that a disk exists at a level $z = P_z$, then there must be 2 endplates above and beneath the disk (if they are not involved by any disease). To detect the endplate above, several slices of $z = P_z - i$ (where i is an integer, $1 \le i \le k$) are evaluated. If one of the $D_{endplate}$ $(P_z - i)$ takes a very low value, it indicates an existence of an endplate nearly above. It is the same near the endplate beneath. Therefore, the function,

$$D_{\text{eval}}(P_z) = D_{\text{disk}}(P_z) - \frac{1}{2}\left[\min_{1\le i\le k} D_{\text{endplate}}(P_z - i) + \min_{1\le i\le k} D_{\text{endplate}}(P_z + i)\right] \tag{8}$$

is expected to take a local maximum at each disk, which is sandwiched by 2 endplates (Fig. 7). The constant k is determined from the expected maximal thickness of the intervertebral disks. We used $k = 3$ for this study. Finally, z coordinates of the disks are determined based on the peak detection of D_{eval}. Following

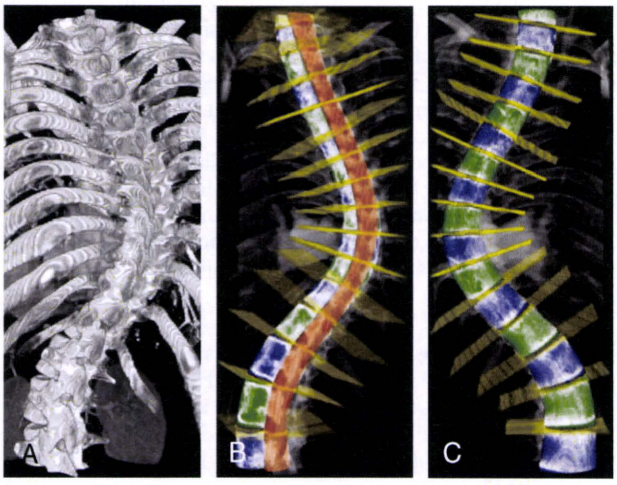

FIGURE 8. A, Segmentation result in the scoliosis case (case 15). B, Volume rendering image of the curved (scoliosis) spine (posterior view). Result of model fitting and disk detection (posterior view). C, Same as B (anterior view).

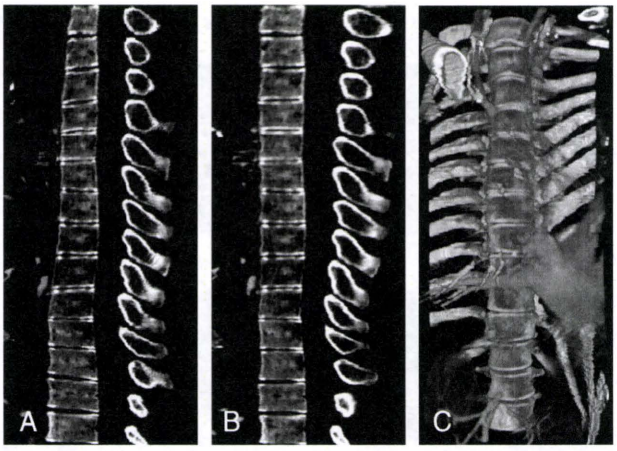

FIGURE 9. Straightened and size-adjusted images based on the segmentation result (the same case as Fig. 9). A, Straightened sagittal image. B, Size-adjusted sagittal image. C, Volume rendering image of the size-adjusted volume data (anterior view).

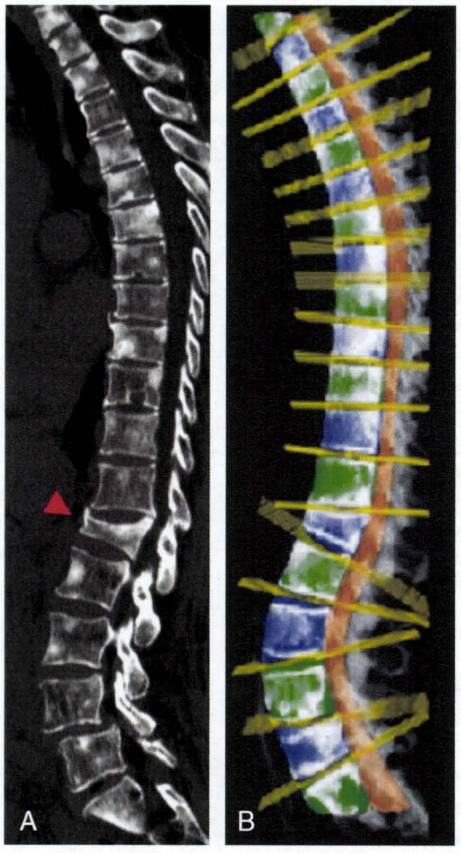

FIGURE 10. A case with bone metastases and compression fracture in L1 (arrowhead; case 9). A, A sagittal image of the original CT data. B, The model-fitting and disk-detection result.

this, the tilt angle of each disk is determined from (n_x, n_y), which maximize D with a given P_z.

Virtual Straightening and Size Adjusting

After model fitting and disk detection, the spine is virtually straightened. The local volume data set including whole spine structures is reconstructed so that all the intervertebral disks are oriented to the axial direction, whereas all the disk intervals are uniform. Size-adjusted images, in which every vertebral body is deformed to be the same size, are also reconstructed.

At first, a set of curved axial images is reconstructed along with the spinal curvature. These reconstructed axial images are tilted so that they align approximately parallel to adjacent intervertebral disks. The number of images between disks is fixed (32 in this study). Following this, a set of size-adjusted images is reconstructed. All tilted axial images are stretched or shrunk along the x and y coordinates so that the elliptic column $\boldsymbol{B}$ becomes a straight cylinder with a constant radius.

RESULT

We applied the proposed method to the clinical CT data of 16 cases: 8 without evident bone disease, 6 with bone metastases, and 2 with scoliosis. These examinations were performed in 2 hospitals, The University of Tokyo Hospital and the Toshiba General Hospital (Tokyo, Japan). The approval of the institutional review board was not required for this retrospective study, following our institutional research policy.

All of the CT images were obtained with a 64–detector row CT (Aquilion 64; Toshiba Medical Systems Corporation, Otawara, Tochigi, Japan), except for one scoliosis case with a single-detector CT (Aquilion; Toshiba Medical Systems Corporation).

The results were evaluated visually by a board-certified radiologist. The model fitting was evaluated as successful if the elliptic column of the model was included and localized within the vertebral column and the vertebral canal. Regarding the disk detection, the evaluation criterion was whether the position and tilt angle of the disk are properly detected. Undetected and improperly detected disks (false disks) were counted. Only disks between T1/2 and L5/S1 were evaluated.

Fitting the model to the thoracic and lumbar spines was successfully carried out, except for a case with a metallic indwelling device placed in the spine (case 10). This case was excluded for further evaluation. Examples of model fitting and curved multiplanar reformation for a scoliosis case (case 15) are shown in Figures 8 (segmentation result) and 9 (normalization result), respectively.

Accuracy of the thoracic and the lumbar intervertebral disk detections was evaluated in the other 15 cases. In the 8 cases without bone disease, 132 disks were detected and 2 were missed. In the 5 metastatic cases, 81 were detected and 1 was missed. All 32 disks were detected in the 2 scoliosis cases. Totally, 5 false disks were detected in 3 cases. Disk detection was successful in the 2 cases with metastases and compression fracture (Fig. 10), except for 1 false disk. The result was summarized in Table 1.

Virtual straightening and size adjusting was performed successfully for 9 of 15 successfully model-fitted cases. In the other 6 cases, nonuniformity of array was observed because of missed or falsely detected intervertebral disk(s).

DISCUSSION

We developed an automated segmentation method for the thoracic and the lumbar vertebral bodies and the spinal canal from the CT data. Our method was proved to be applicable to cases with scoliosis or metastases. Previous investigators have presented a number of segmentation techniques for the spine, but most of them were limited to the lumbar spine.[12–14] Yao et al[4] have reported and evaluated a segmentation method for the spine with bone metastases. However, no spinal segmentation method has been evaluated with clinical CT data of scoliosis so far.

Our method is based on a model composed of 2 deformable elliptic columns. Therefore, the method is classified in the group of deformable model–based approaches.[9] In our model, the segmented structure is reconstructed as a simple geometric representation (ie, elliptic columns) controlled by a small number of parameters. This feature showed great advantage in application for virtual normalization because the model properties, such as medial axes of columns, could be used for nonrigid transformation of the volume data. Another advantage of our method is that the elliptic column model was designed with enough flexibility for fitting to the spine with a possible pathologic condition such as scoliosis, lordosis, kyphosis, and compression fracture.

One of our goals for spinal segmentation is CAD of spinal bone metastases. Automated or semiautomated methods for CT[3,15] and magnetic resonance imaging[16] have been reported. One of the preliminary CAD systems showed a fair sensitivity of 0.83 to 0.94 but yielded 3 false negatives among 28 lesions, mainly because of an unsuccessful data-driven segmentation of the spine.[3] Our model-based approach is expected to improve the problem based on normalized spine volume data. Currently, our method performs only partitioning of each vertebral body. Additional algorithm for identifying whole vertebrae is needed

TABLE 1. Clinical Information and Segmentation Results of the Cases

Case	Age and Sex	Malignancy	Voxel Size, mm		Vertebrae	Result			Note
			x/y	*z*	Included	Model Fitting	Disk Detection	False Disk	
Cases without bone disease									
1	65, male		0.71	1.00	T1-L5	Successful	17/17		
2	44, male		0.70	1.00	T1-L4	Successful	15/16		
3	63, male		0.68	1.00	C7-L5	Successful	17/17		
4	78, male		0.67	1.00	C7-L5	Successful	16/17	2	
5	60, male		0.72	1.00	T1-L5	Successful	17/17		
6	63, female		0.63	1.00	C2-L5	Successful	17/17	2	
7	64, male		0.98	1.25	C1-L5	Successful	17/17		
8	63, male		0.98	1.25	C1-L5	Successful	16/17		
Cases with bone metastases									
9	73, female	Ovarian carcinoma	0.63	0.80	T1-L5	Successful	17/17		Compression fracture in L1
10	44, male	Renal cell carcinoma	0.63	1.00	C1-L5	Failed			Metal device placed in the spine
11	71, male	Adenocarcinoma of the parotid grand	0.61	1.00	C1-L3	Successful	14/15		
12	53, female	Breast carcinoma	0.67	1.00	C6-L4	Successful	16/16	1	Compression fracture in L1
13	64, male	Pancreas carcinoma	0.63	1.00	C1-L5	Successful	17/17		
14	71, male	Colon carcinoma	0.68	1.00	T1-L5	Successful	17/17		
Cases with scoliosis									
15	28, male		0.61	0.80	T1-L3	Successful	15/15		
16	19, female		0.39	1.25	C7-L4	Successful	17/17		
Total						15/16	245/249	5	

in such a CAD application. However, it is not a difficult task because all vertebral bodies were already partitioned and their tilt and rotation angles were also estimated.

We also presented an automated curved multiplanar reformation algorithm. Unlike the previously reported method,[17] our method detects the intervertebral disks, so that the images are reconstructed to be perpendicular (for sagittal and coronal images) or parallel (for axial images) to the disks. In the images for 2 patients with scoliosis, deformation of the spine was almost cancelled. Therefore, our elliptic column model may be enough to describe most spinal deformities in scoliosis and, possibly, in lordosis or kyphosis, although further research with more cases will be required. Clinically, it is expected that an automated deformity measurement for CT datasets might bring more reliable and reproducible information for scoliosis than conventional Cobb angle measurement based on 2D radiographs with manual[18] or computer-based[19,20] measurement.

Our future work covers cervical intervertebral disk detection. To the best of our knowledge, no segmentation method of the spine has been evaluated for cervical vertebrae, except for one study that reported a semiautomatic segmentation method for the C1 to the C3 vertebrae only.[21] Because the cervical vertebrae are relatively small and the intervertebral spaces are narrow, disk detection is not a simple task and improvement of the disk detection scheme is needed.

In conclusion, we developed an automated segmentation method for the thoracic and the lumbar spines from CT images based on a deformable model. The method was validated by using data sets of 16 clinical cases. As one of the clinical applications, virtual straightening and size adjusting is performed automatically based on the segmentation results. Through the study, our segmentation method is proved to be feasible in clinical cases even with bone diseases, such as scoliosis and bone metastases.

ACKNOWLEDGMENT

The authors would like to thank Dr. Kaworu Kojima for providing CT datasets.

REFERENCES

1. Létourneau D, Kaus M, Wong R, et al. Semiautomatic vertebrae visualization, detection, and identification for online palliative radiotherapy of bone metastases of the spine. *Med Phys*. 2008;35:367–376.
2. Mastmeyer A, Engelke K, Fuchs C, et al. A hierarchical 3D segmentation method and the definition of vertebral body coordinate systems for QCT of the lumbar spine. *Med Image Anal*. 2006;10:560–577.
3. O'Connor SD, Yao J, Summers RM. Lytic metastases in thoracolumbar spine: computer-aided detection at CT—preliminary study. *Radiology*. 2007;242:811–816.
4. Yao J, O'Connor SD, Summers RM. Automated spinal column extraction and partitioning. In: *Proceedings of the Third IEEE International Symposium on Biomedical Imaging*. 2006:390–393.
5. Roodman GD. Mechanisms of bone metastasis. *N Engl J Med*. 2004;350:1655–1664.
6. Hedequist D, Emans J. Congenital scoliosis: a review and update. *J Pediatr Orthop*. 2007;27:106–116.
7. Resnick D. Degenerative diseases of the vertebral column. *Radiology*. 1985;156:3–14.

8. Kass M, Witkin A, Terzopoulos D. Snakes: active contour models. *Int J Comput Vis*. 1988;1:321–331.
9. McInerney T, Terzopoulos D. Deformable models in medical image analysis: a survey. *Med Image Anal*. 1996;1:91–108.
10. Press WH, Teukolsky SA, Vetterling WT, et al. *Numerical Recipes in C++. The Art of Scientific Computing*. 2nd ed. Cambridge, UK: Cambridge University Press; 2002.
11. Lohmann G. *Volumetric Image Analysis*. Chichester, England: John Wiley & Sons Ltd; 1998.
12. Herring JL, Dawant BM. Automatic lumbar vertebral identification using surface-based registration. *J Biomed Inform*. 2001;34:74–84.
13. Ghebreab S, Smeulders AW. Combining strings and necklaces for interactive three-dimensional segmentation of spinal images using an integral deformable spine model. *IEEE Trans Biomed Eng*. 2004;51: 1821–1829.
14. Tan S, Yao J, Ward MM, et al. Level set based vertebra segmentation for the evaluation of ankylosing spondylitis. *SPIE Medical Imaging*. 2006;6144:614407.
15. Whyne C, Hardisty M, Wu F, et al. Quantitative characterization of metastatic disease in the spine. Part II. Histogram-based analyses. *Med Phys*. 2007;34:3279–3285.
16. Jerebko AK, Schmidt GP, Zhou X, et al. Robust parametric modeling approach based on domain knowledge for computer aided detection of vertebrae column metastases in MRI. *Inf Process Med Imaging*. 2007;20:713–724.
17. Vrtovec T, Likar B, Pernus F. Automated curved planar reformation of 3D spine images. *Phys Med Biol*. 2005;50:4527–4540.
18. Adam CJ, Izatt MT, Harvey JR, et al. Variability in Cobb angle measurements using reformatted computerized tomography scans. *Spine*. 2005;30:1664–1669.
19. Chockalingam N, Dangerfield PH, Giakas G, et al. Computer-assisted Cobb measurement of scoliosis. *Eur Spine J*. 2002;11:353–357.
20. Cheung J, Wever DJ, Veldhuizen AG, et al. The reliability of quantitative analysis on digital images of the scoliotic spine. *Eur Spine J*. 2002; 11:535–542.
21. Shi H, Scarfe WC, Farman AG. Cervical vertebrae segmentation from cone beam CT datasets. *Int J CARS*. 2006;1:531.

Transactions on Mass-Data Analysis
of Images and Signals
Vol. 2, No. 1 (2010) 112-127
©ISSN:1868-6451 (Journal),
ISBN: 978-3-940501-13-4,
IBaI Publishing ISSN 1864-9734

ibai Publishing
www.ibai-publishing.org

CIRCUS: an MDA Platform for Clinical Image Analysis in Hospitals

Yukihiro Nomura[1], Naoto Hayashi[2], Yoshitaka Masutani[1,3], Takeharu Yoshikawa[2], Mitsutaka Nemoto[1], Shouhei Hanaoka[1], Soichiro Miki[3], Eriko Maeda[2], and Kuni Ohtomo[1,3]

[1] Department of Radiology, The University of Tokyo Hospital, 7-3-1 Hongo, Bunkyo-ku, Tokyo 113-8655, Japan
[2] Department of Computational Diagnostic Radiology and Preventive Medicine, 22nd Century Medical and Research Center, The University of Tokyo Hospital 7-3-1 Hongo, Bunkyo-ku, Tokyo 113-8655, Japan
[3] Division of Radiology and Biomedical Engineering,Graduate School of Medicine, The University of Tokyo, 7-3-1 Hongo, Bunkyo-ku, Tokyo 113-8655, Japan
nomuray-tky@umin.ac.jp

Abstract. For mass image data analysis in hospitals, we have built an integrated platform for the development and assessment of various types of image analysis software such as computerized detection of lesions. It mainly consists of a set of clinical image databases, and a clinical server with web-based interfaces for launching analysis software and for viewing and evaluating analysis results. The image databases are employed for the registration of a sufficient number of clinical cases for machine learning in computer-assisted detection/diagnosis (CAD) software development. In addition, the clinical server collects data for evaluating the interpretation performance of radiologists as well as that of the CAD software.

Keywords: computer-assisted detection/diagnosis (CAD), image database system, web-based clinical server, on-line learning

1 Introduction

A large number of images are generated by imaging devices in hospitals. The number of images is usually from 300 to 500 (and sometimes over 1,000) per examination and is increasing year by year. Hence, the workload of radiologists

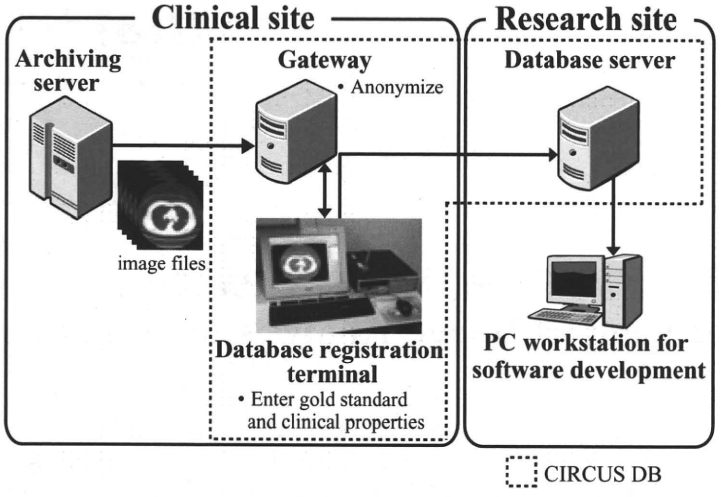

Fig. 1. Configuration of CIRCUS DB for collecting clinical cases with pixel-based gold standard data sets. CIRCUS DB includes a gateway, a database registration terminal, and a database server.

has been increasing. In addition, there are differences between the interpretation performance of radiologists. Therefore, computer-assisted detection/diagnosis (CAD) software is expected to assist radiologists.

The development of CAD software involves a cycle of algorithm development, software implementation, clinical use, and refinement of the algorithm and the software based on clinical evaluation. This cycle is expected to accelerate the development of CAD software. However, there are currently problems in CAD software development.

In algorithm development, a sufficient number of clinical cases are required to ensure the higher reliability of CAD software. In addition, the database must include pixel-based gold standard data sets for supervised learning in CAD software.

The clinical use of a CAD system requires on-line processing in the clinical image network, the retrieval of images from an imaging device or an archiving server, and the display of results obtained from the CAD software on interpretation terminals. In recent years, several research groups have reported CAD servers based on on-line processing of CAD software [1–4], which are aimed at improvement of diagnostic workflow and at clinical decision support. For example, Martinelli, et al. [4] reported an integrated platform dedicated to chronic heart failure, including web-based interfaces for analyzing echocardiograms and a knowledge-based decision support system. A commercial CAD server (syngo.via; Siemens Healthcare, Erlangen, Germany) has also been released. However, these systems might lack viewpoints of tuning and improvement of CAD software performance in an efficient way.

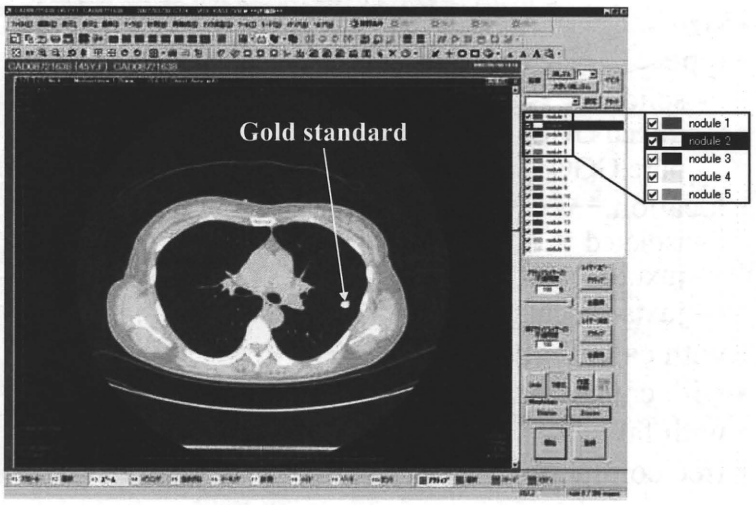

Fig. 2. Interface for pixel-based gold standard labeling. The arrow indicates the labeled gold standard. Gold standard is painted in colors depending on the categorization of each region.

Clinical images have different properties depending on imaging devices, in terms of pixel size, slice thickness, signal-to-noise ratio, field of view, and others. It is important to adapt CAD software to various imaging configurations based on incremental learning. Previously, CAD software has been developed for off-line applications [5]. Thus, if new clinical cases are collected, relearning incorporating the additional cases must be carried out. However, it is difficult to collect additional cases due to the protection of personal information in hospitals. Therefore, a strategy for the on-line learning of CAD software in clinical environment is important. To refine or adapt CAD software based on on-line learning, it is required to evaluate whether or not the results obtained from CAD software are appropriate on the basis of a clinical diagnosis and to realize on-line learning based on evaluations.

To solve the above problems in CAD software development, we have been building an integrated system for the development, clinical use, evaluation, and refinement of CAD software as a mass data analysis (MDA) platform for clinical image analysis in hospitals. The system was named CIRCUS (clinical infrastructure for radiologic computation of united solutions).

2 System Description

We have built two types of subsystem for CAD software development. First, we built an image database system with an interface for pixel-based gold standard labeling to effectively collect a sufficient number of clinical cases with pixel-based gold standard data sets. In addition, we also built a web-based clinical server to

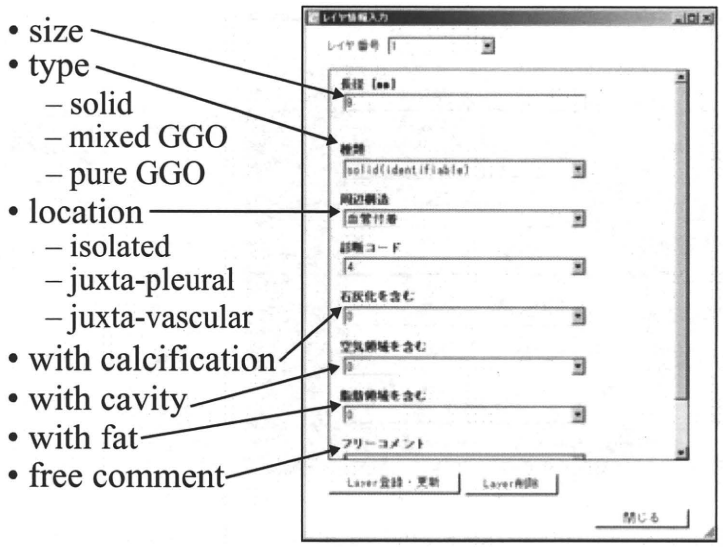

Fig. 3. Interface for entry of clinical properties in database of lung nodules. The properties of lung nodules are size, type, location, calcification, cavity, and fat, and an additional space is provided for comments (GGO: ground glass opacity).

realize the on-line processing of CAD software and interfaces for evaluating CAD results and for on-line learning. We named the image database system CIRCUS DB and the web-based clinical server CIRCUS CS.

2.1 CIRCUS DB (Image Database System)

CIRCUS DB includes a gateway, a database registration terminal, and a database server (Fig. 1). The gateway retrieves image files from an archiving server based on requests from the database registration terminal, and then anonymizes the image files. At the database registration terminal, pixel-based gold standard and clinical properties are entered using interface windows. After these processes, anonymized image files with gold standard and clinical properties are registered in the database server. At the research site, image files with gold standard data are retrieved upon request for software development. Clinical properties are also retrieved as comma-separated values (CSV) files.

Interfaces for Labeling Pixel-based Gold Standard and for Entering Clinical Properties. Pixel-based gold standard is semiautomatically or manually labeled on each 2D image using a mouse or pen tablet. Figure 2 shows an interface for gold standard labeling. Gold standard is painted in colors depending on the categorization of each region. For example, benign lung nodules are painted in yellow, and malignant lung nodules are painted in red. Labeled

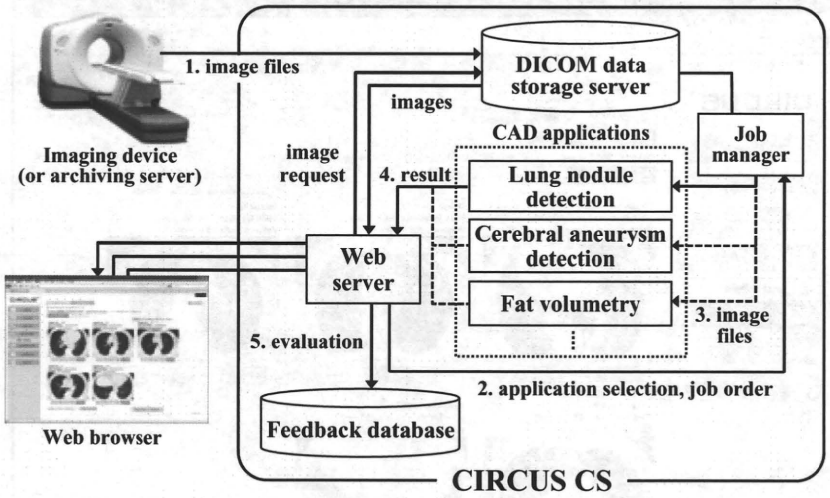

Fig. 4. Configuration of CIRCUS CS for on-line processing of CAD software and evaluating CAD results. CIRCUS CS includes a DICOM data storage server, a job manager, a web server, and a feedback database. CAD applications are provided as plug-ins of CIRCUS CS.

gold standard data are saved as digital imaging and communications in medicine (DICOM) overlays with up to 16 layers. After that, clinical properties are entered using an interface window (Fig. 3). Various clinical properties are set for each database. For example, the properties of lung nodules are their size, type, location, calcification, cavity, and fat, and an additional space is provided for comments.

2.2 CIRCUS CS (Clinical Server with Web Interface)

Figure 4 shows the configuration of CIRCUS CS. The processing procedures of CIRCUS CS are described as follows.

1. Image files are transferred from an imaging device or an archiving server to a DICOM data storage server.
2. The user selects a CAD application via a web browser and then registers a job order.
3. The job manager process the selected application.
4. The results obtained from the CAD application and interfaces for evaluation (clinical feedback) are displayed as a web page.
5. Radiologists evaluate the results from the CAD application on the basis of a diagnostic decision, and the entered evaluations are registered in the feedback database.

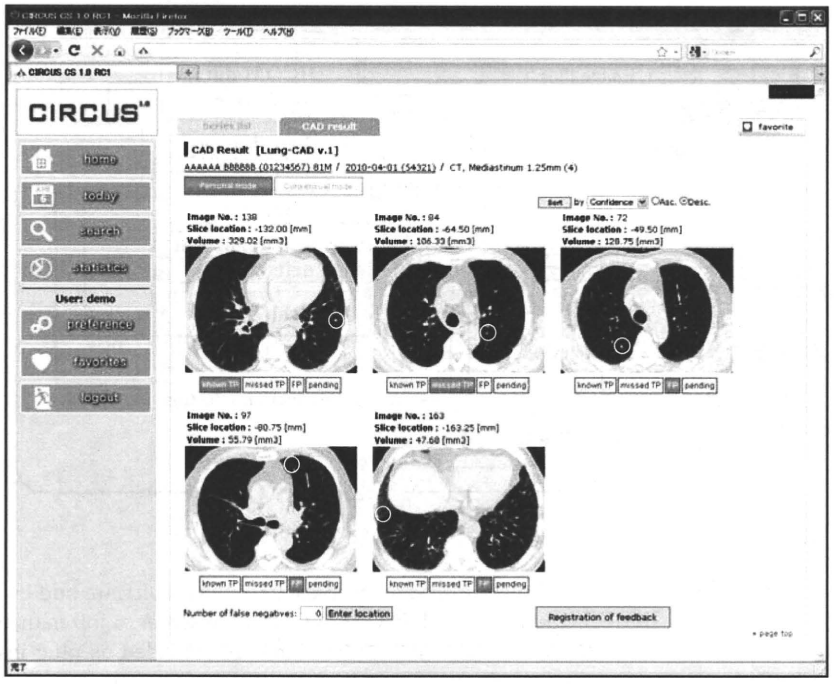

Fig. 5. Result of lung nodule detection in CT images. The center slice of the lesion candidate and radio buttons (as a feedback interface) are displayed for each lesion candidate. Circles indicate the locations of lesion candidates.

CAD applications are provided as plug-ins of CIRCUS CS. Our CAD applications are outlined below.

- Lesion detection applications: cerebral aneurysm detection in magnetic resonance (MR) angiograms [6], lung nodule detection in chest computed tomography (CT) images [7], skin lesion detection in whole-body ^{18}F-fluorodeoxy-glucose positron emission tomography/computed tomography (FDG-PET/CT) images [8]
- Visualization application: virtual straightening of spine in whole-body CT images [9]
- Measurement application: volumetry of visceral fat tissue (VAT) and subcutaneous fat tissue (SAT) in whole-body CT images

The user logs in to CIRCUS CS using his/her individual user ID and password. The individual login enables us to adjust a set of displayed lesion candidates adaptively for each user. In addition, it also enables the collection of personal diagnostic decision data for each radiologist. On the basis of the collected data, the interpretation performance of the radiologist can be evaluated.

Figure 5 shows a result of lung nodule detection in chest CT images. The center slice of the lesion candidate and radio buttons (as a feedback interface) are

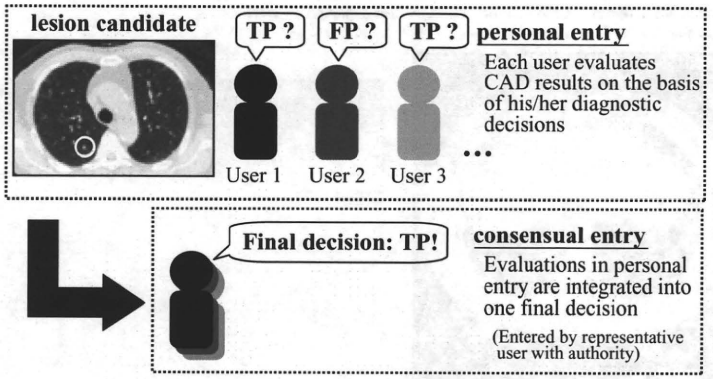

Fig. 6. Two stages of clinical feedback entry.

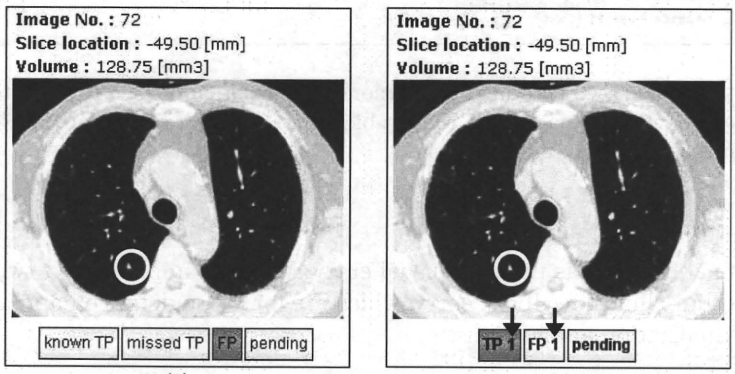

Fig. 7. Radio buttons used to classify displayed candidates. (a) Personal entry, (b) consensual entry. The arrows indicate the number of users entered in the personal entry.

displayed for each lesion candidate. Lesion candidates are displayed in descending order of likelihood, and the number of displayed lesion candidates is adjusted by each user. In Fig. 5, the top five lesion candidates are displayed. Hereafter, the displayed lesion candidates are referred to "displayed candidates", and other potential candidates are referred to "undisplayed candidates".

2.3 Interfaces for Clinical Feedback

Radiologists evaluate the results obtained from the CAD application on the basis of a diagnostic decision. The feedback entry in our system includes two stages: a personal entry and a consensual entry (Fig. 6). In the personal entry, each radiologist can evaluate the result obtained from the CAD application. Evaluations in the personal entry by two radiologists (or more) are integrated

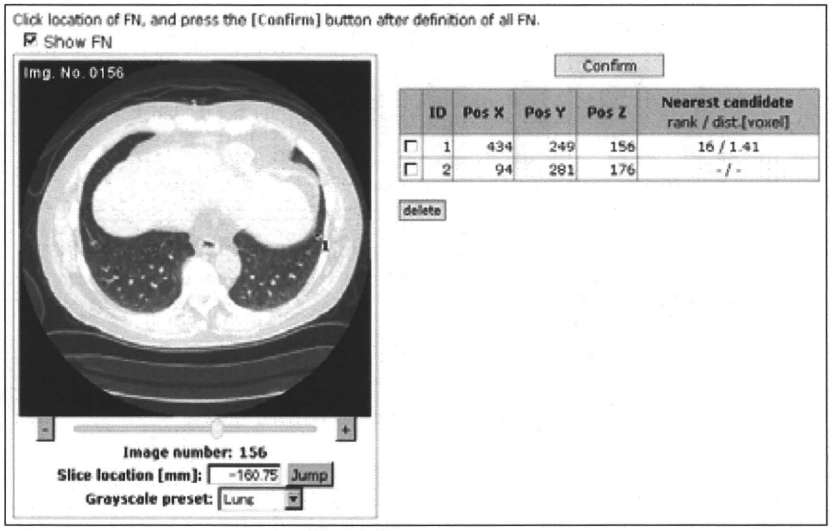

Fig. 8. Interface for used entering FN locations. The location of each FN is entered by clicking on the left 2D image. The right table shows the coordinates of the FNs and the existence of undisplayed candidate.

into one final decision as the consensual entry. We have implemented two types of interface for clinical feedback entry, which are for lesion detection applications and for visualization applications.

Interfaces for Lesion Detection Applications. The interfaces for lesion detection applications include radio buttons to classify displayed candidates and an interface for entering the locations of false negative (FN). Figure 7 (a) shows radio buttons used to classify displayed candidates in the personal entry. Each displayed candidate is classified as follows:

- known true positive (TP): lesion detected by radiologist's interpretation without CAD application
- missed TP: lesion missed in radiologist's interpretation without CAD application
- false positive (FP): false positive of the CAD application
- pending: difficult to classify into a TP or FP

Figure 7 (b) shows radio buttons used in the consensual entry. The number of radiologists at the personal entry is displayed in the radio buttons (arrows in Fig. 7 (b)). In the consensual entry, known TPs and missed TPs are usually integrated into TPs.

In the interface used for entering the location of FN, a 2D image including an FN is first selected using a slider control (Fig. 8). After clicking on the location

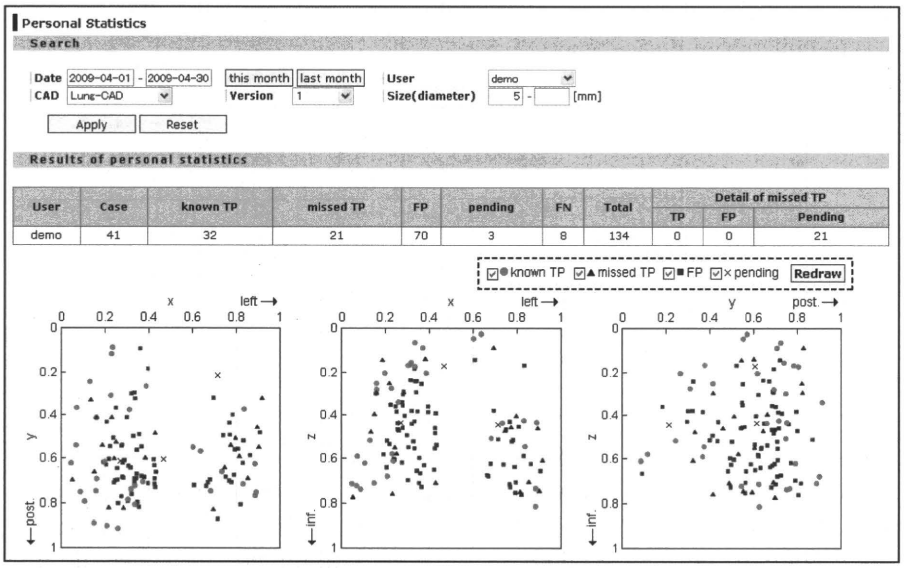

Fig. 9. Interface showing interpretation characteristics in lung nodule detection. The interface shows a table of classifications of lesion candidates and scatter plots of the classification results. Each classification in the scatter plots can be shown or hidden using check boxes (dashed box).

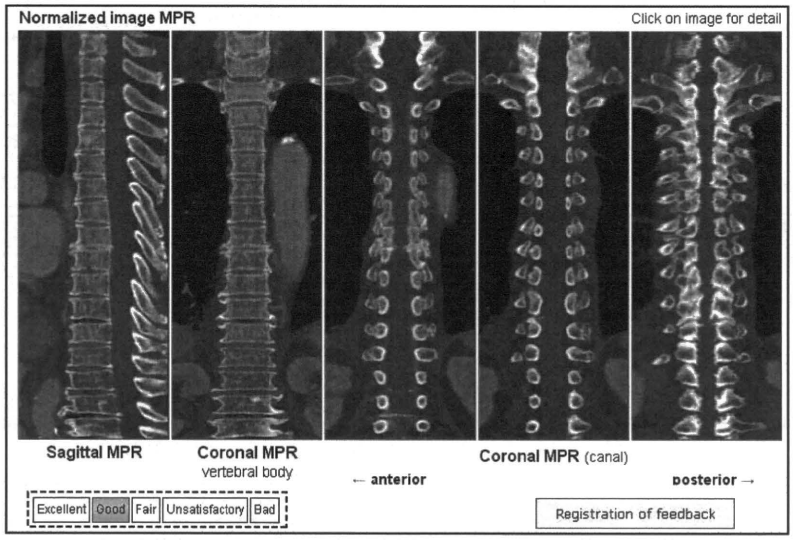

Fig. 10. Result of virtual straightening of spine in whole-body CT images with feedback interface for entering visual score (dashed box).

Table 1. Average times required for data retrieval at research site.

Type of database	Image type	Size	Time [sec]	File size [MB]	
				original image	gold standard
Cerebral aneurysm	MR(A)	512×512×132	45	69.2	34.6
Lung nodule	CT	512×512×250	80	131.0	65.5
Skin lesion	CT*	512×512×275	95	144.2	72.1
	CT**	512×512×717	180	375.9	-
	PET	128×128×275	10	9.0	-
Visceral space	CT	512×512×717	240	375.9	375.9

* Slice thickness: 3.75mm (for gold standard lebeling)
** Slice thickness: 1.25mm (for processing)

of FN, its coordinates and the existence of undisplayed candidate are added to a table.

Accumulated clinical feedback, which includes the classification of displayed candidates and the locations of FNs, can be used to evaluate the performance of the CAD software and to refine the software. For radiologists, collecting data on personal entry including the number of missed lesions makes it possible to investigate individual differences in interpretation performance. We have also implemented an interface showing the interpretation characteristics of each user based on his/her clinical feedback (Fig. 9). The interface shows a table of clas-

Table 2. Average times required for transfer of image files and processing of CAD applications.

CAD application	Image type	Size	No. of images	Time for transfer [sec]	Time for processing [sec]	Total [sec]
Cerebral aneurysm detection	MR(A)	512×512	152	15	45	60
Lung nodule detection	CT	512×512	250	20	185	205
Skin lesion detection	CT	512×512	717	50	270	330
	PET	128×128	275	10		
Vertebral deformity analysis	CT	512×512	717	50	220	270
Volumetry of VAT and SAT	CT	512×512	717	50	380	430

sifications of lesion candidates and scatter plots of the classification results. The coordinates of the scatter plots are normalized by target volumes. Each classification in the scatter plots can be shown or hidden using check boxes.

Interface for Visualization Applications. Figure 10 shows an example of a feedback interface for visualization applications. The user enters a visual score using radio buttons. The visual score is divided into five levels: excellent, good, fair, unsatisfactory, and bad.

3 Results

The specifications of our platform including the databases and servers are shown below.

- Gateway: Intel Dual Xeon 1.86 GHz dual processor with 3 GB RAM, and Microsoft Windows Server 2003 operating system
- Database registration terminal: Intel Pentium D 3.40 GHz with 2 GB RAM, and Microsoft Windows XP Professional operating system
- Database server: Intel Dual Xeon 1.86 GHz dual processor with 3 GB RAM, Microsoft Windows Server 2003 operating system, and MySQL 5.0.45
- Clinical server: Intel Quad Xeon 2.0 GHz with 4 GB RAM, Microsoft Windows Server 2003 operating system, Apache 2.2.15, Open SSL 0.9.8m, PostgreSQL 8.4.4, and DCMTK 3.5.4 [10]

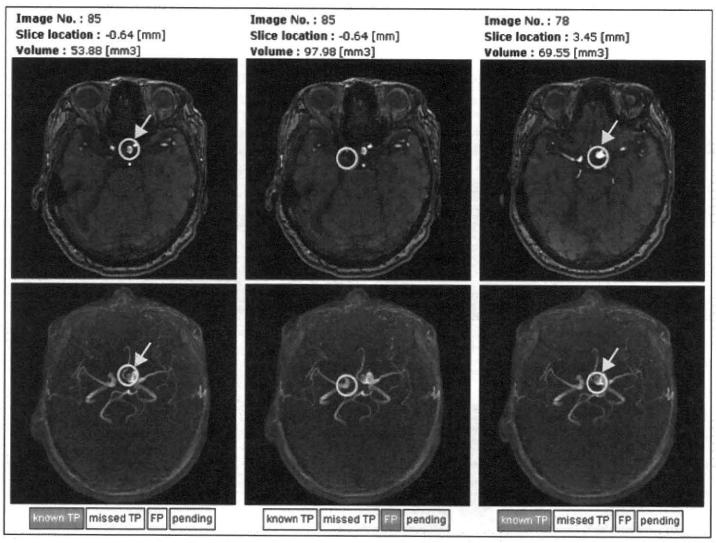

Fig. 11. Result of cerebral aneurysm detection in MR angiograms. The upper images show the center slice of the displayed candidate, the lower images show the maximum-intensity projection. The circles indicate the location of the lesion candidate, and the circles with an arrow indicate the detected cerebral aneurysm.

We built four types of image databases: 1) cerebral aneurysms in MR angiograms, 2) lung nodules in chest CT images, 3) skin lesions detection in whole-body FDG-PET/CT images, and 4) visceral spaces in whole-body CT images. The present databases included 1,061 cases of cerebral aneurysms, 111 cases of lung nodules, 37 cases of skin lesions, and 26 cases of visceral spaces. In the database for lesion detection applications, the average time required for gold standard labeling,